Organisation of self-assembling peptide nanostructures into macroscopically ordered lamella-like layers by ice crystallisation†‡

Shane Scanlon,[a] Amalia Aggeli,*[a] Neville Boden,[a] Tom C. B. McLeish,[b] Peter Hine,[c] Rudy J. Koopmans[d] and Cyrus Crowder[e]

Received 5th September 2008, Accepted 5th January 2009
First published as an Advance Article on the web 24th February 2009
DOI: 10.1039/b815558e

Bio-inspired molecular self-assembly has attracted considerable research interest as a promising route to novel nanostructured materials. Self-assembling peptides have proven particularly popular building blocks for the construction of a variety of well-defined nanostructures. There is a great interest in learning to control not only the types and properties of nanostructures, but also their precise macroscopic organisation. Here we investigate the effect of water crystallisation during freezing as a possible method for directed organisation of preformed β-sheet tapes, ribbons and fibrils and for the production of microporous materials comprising lamella-like layers. We employ a range of short, systematically designed self-assembling peptides and a wide variety of techniques including SEM, TEM, X-ray tomography, X-ray diffraction, FTIR spectroscopy and compression testing. We find that ice growth does not alter the peptide nanostructures but templates the formation of lamella-like layers of mesoscopically aligned peptide ribbons and fibrils into nematic-like domains. The lamella are macroscopically oriented into regularly spaced stacks, giving rise to rather brittle peptide aerogels. This behaviour is contrasted with that of other self-assembling networks such as surfactant rod-like micelles and the polysaccharide agar. The differences in the properties of the self-assembling network seem to prescribe the way it will behave during ice crystallisation, and whether or not it will form ordered lamella structures. This approach may lead to the preparation of well-aligned peptide nanostructures, important for high-resolution structural studies; anisotropic microporous materials comprising lamella-like layers of self-assembling peptide fibrils with incorporated protein-like bioactivity may also be useful in medical applications e.g. tissue engineering, and nanotechnology.

Introduction

Bio-inspired molecular self-assembly has attracted considerable research interest in recent years as a promising route to novel nanostructured materials for the chemical and pharmaceutical industries and in nanotechnology.[1–5] Self-assembling peptides have proven particularly popular building blocks for the construction of a wide range of well-defined nanostructures, such as μm-long fibrils, vesicles and tubes.[6] Peptides have a number of appealing properties, such as production by chemical synthesis or biotechnology, chemical versatility,[7–10] incorporation of protein-like bioactivity as well as precise and intrinsic ability for self-assembly; for example even very simple homopolypeptides such as poly-L-threonine were shown to self-assemble into long cross β-sheet ribbons in water.[11] We previously developed one of the simplest known model peptide systems which, above a critical concentration (c*) in solution, undergo nucleated one-dimensional self-assembly from monomeric random coil into a hierarchy of well-defined μm-long β-sheet aggregates, such as helical tapes (one molecule in thickness), ribbons (double tapes), fibrils (stacks of ribbons) and fibres (entwined fibrils) as a function of increasing peptide concentration (Fig. 1).[12] The aggregates are twisted due to the chirality of the peptide molecules. These peptide structures are thoroughly characterised, well understood and offer a well-defined model system to study peptide self-assembly under a variety of conditions. An example of a tape-forming peptide in water is P_{11}-1 (Table 1) whose primary structure consists of 11 amino acids and is made up of the predominantly hydrophilic amino acid residue glutamine (Gln). The critical concentration of P_{11}-1 for self-assembly in water is ~15 μg/ml. P_{11}-2 is a variant of P_{11}-1 in which three glutamines of P_{11}-1 at positions 4, 6 and 8 were replaced with three hydrophobic amino acids, one tryptophan (Trp) and two phenylalanines (Phe) (Table 1). P_{11}-2 forms amphiphilic tapes in water with a c* of ~75 μg/ml. The tapes stack together *via* their hydrophobic sides to form ribbons which in turn give rise to fibrils

[a]*Centre for Self-Organising Molecular Systems (SOMS Centre), School of Chemistry, University of Leeds, Leeds, UK LS2 9JT. E-mail: a.aggeli@leeds.ac.uk; Fax: +44 (0)113 343 6452; Tel: +44 (0)113 343 6407*
[b]*Depts. of Physics and Chemistry, University of Durham, South Road, Durham, UK DH1 3LE*
[c]*School of Physics and Astronomy, University of Leeds, Leeds, UK LS2 9JT*
[d]*Dow Europe GmbH, Wolleraustrasse 15-17, 8807 Freienbach, Switzerland*
[e]*ICDD, 12 Campus Blvd., Newtown Square, PA-19073, U. S. A.*

† This paper is part of a *Soft Matter* theme issue on Self-Assembly. Guest editor: Bartosz Grzybowski.

‡ Electronic supplementary information (ESI) available: Characterisation of self-assembling peptide aerogels. See DOI: 10.1039/b815558e

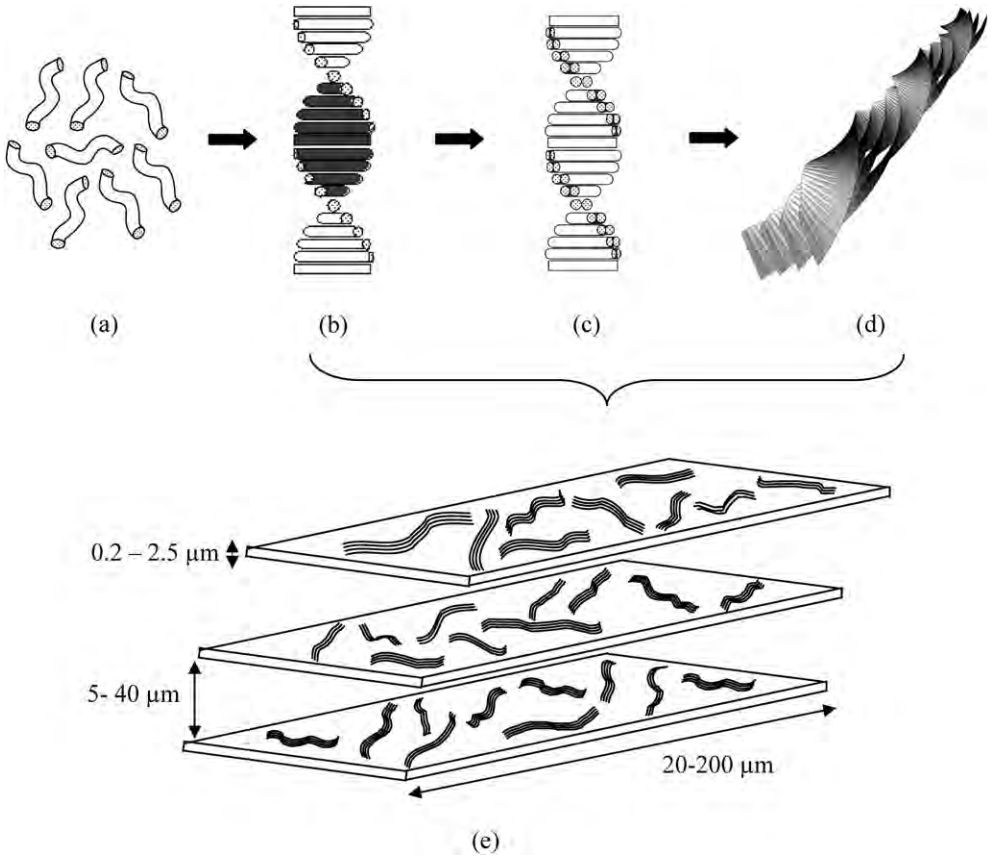

Fig. 1 Illustration of the 1-dimensional self-assembly of peptides represented as rods: (a) random coil monomers, (b) β-sheet tapes, (c) ribbons and (d) fibrils; (e) schematic depicting the packing of nematic-like domains of tapes, ribbons or fibrils into flat lamellar structures after freeze-drying.

Table 1

Peptide	Primary structure
P_{11}-1	CH_3CO-Gln-Gln-Arg-Gln-Gln-Gln-Gln-Gln-Glu-Gln-Gln-NH_2
P_{11}-2	CH_3CO-Gln-Gln-Arg-Phe-Gln-Trp-Gln-Phe-Glu-Gln-Gln-NH_2
P_{11}-4	CH_3CO-Gln-Gln-Arg-Phe-Glu-Trp-Glu-Phe-Glu-Gln-Gln-NH_2
P_{11}-5	CH_3CO-Gln-Gln-Orn-Phe-Orn-Trp-Orn-Phe-Gln-Gln-Gln-NH_2
P_{11}-7	CH_3CO-Ser-Ser-Arg-Phe-Ser-Trp-Ser-Phe-Glu-Ser-Ser-NH_2
P_{11}-8	CH_3CO-Gln-Gln-Arg-Phe-Orn-Trp-Orn-Phe-Glu-Gln-Gln-NH_2

(Fig. 1). Although the ribbons are more flexible than the fibrils and fibres, all these aggregates are rigid enough to behave like semi-rigid rods. Thus at concentrations typically higher than 1 mg/ml, their solutions undergo an isotropic to nematic transition, giving rise to micro-domains of aligned ribbons or fibrils and birefringent solutions.[13] At even higher concentrations, typically >5 mg/ml, the peptide aggregates establish an interconnected 3D network and turn their solutions into self-supporting organogels or hydrogels which can be triggered on and off by external chemical (*e.g.* pH) or physical (*e.g.* temperature) stimuli.[4,14–16] These self-assembling peptides have been explored as promising candidates in a variety of applications, such as templates for nanostructured inorganic materials including hollow silica nanotubes,[17] biomineralisation for *e.g.* dental applications,[18] surface nanocoatings[19] and lubricants for early-stage osteoarthritis.[20]

More recently peptide hydrogels have also been used to produce peptide aerogels by freeze-drying (FD) (lyophilisation).[21,22] This involves freezing a hydrogel and then placing it into a freeze-drier where the surrounding pressure is reduced to an adequate level so that the ice is sublimed directly from the solid to the gas phase.[23] Bio-inspired aerogels have attracted interest for applications such as tissue engineering,[24–27] biosensors[28] and biodegradable packaging.[29] It also became apparent[21] that freeze-drying had a profound effect on the architecture of the peptide gel network by reorganising it into lamellar structures. There is great interest in learning how to control the precise macroscopic organisation of self-assembling nanostructures as advances in this area would make these materials more useful in nanotechnological applications.[30–33] Here we investigate the effect of water crystallisation during freezing as a possible method for the macroscopic organisation of preformed peptide tapes, ribbons and fibrils and also for the production of anisotropic microporous peptide-based materials comprising a lamellar architecture. A range of systematically designed model self-assembling peptides P_{11}-1, P_{11}-2, P_{11}-7 and their variants were studied as well as the homopolypeptide poly-L-threonine (polyT). Following lyophilisation, the peptides were characterised by a wide variety of techniques including SEM, TEM, X-ray tomography, X-ray diffraction, FTIR spectroscopy and compression testing.

Experimental section

Materials

The peptides P_{11}-1, P_{11}-2, P_{11}-4, P_{11}-5, P_{11}-7 and P_{11}-8 were purchased from NeoMPS Groupe SNPE (Strasburg, France) or SynPep, Dublin, California, USA. The peptides were prepared using standard solid phase chemistry and purified by reversed-phase high performance chromatography (HPLC). Peptide quality control was carried out using mass spectrometry, analytical HPLC, amino acid and elemental analysis (carbon, hydrogen, nitrogen and fluorine) and UV spectroscopy. Theoretical masses were calculated to be 1497 Da (P_{11}-1), 1594 Da (P_{11}-2), 1596 Da (P_{11}-4), 1522 Da (P_{11}-5), 1348 Da (P_{11}-7) and 1567 Da (P_{11}-8). The mass found for each purified peptide was the same as the theoretical mass. HPLC purity (wavelength 210 nm) was measured to be 88% (P_{11}-1), 96% (P_{11}-2), 96% (P_{11}-4), 95% (P_{11}-5), 95% (P_{11}-7) and 96% (P_{11}-8). The peptide content was found to be 87% (P_{11}-1), 87% (P_{11}-2), 93% (P_{11}-4), 93% (P_{11}-7) and 77% (P_{11}-8); the remaining dry mass was counterions (mainly ammonium counterions bound on negatively charged peptides and trifluoroacetate counterions bound on positively charged peptides) and residual bound water. Poly-L-threonine (MW 7600) and gelatin (porcine skin, for electrophoresis—300 Bloom) were purchased from Sigma Aldrich Ltd, Gillingham, Dorset, UK, whilst agar was purchased from Park Scientific, Northampton, UK. Glutaraldehyde (GA) grade I 70% in H_2O, potassium bromide, cetyltrimethylammonium chloride (CTAC), sodium salicylate and sodium chloride were purchased from Sigma Aldrich Ltd, Gillingham, Dorset, UK. Dulbecco's modified Eagle's medium (DMEM), was purchased from Invitrogen/Life Technologies Limited, Paisley, UK.

Sample preparation

Hydrogels were prepared by dissolution of the chosen peptide in 18.2 MΩ Milli-Q deionised water. 0.5 or 1 ml samples were prepared in glass vials by mixing the dry peptide with the appropriate amount of water. Once prepared the samples were vortexed in order to ensure complete homogeneity, and left at room temperature for a week in order to equilibrate. GA-treated hydrogels were prepared by producing a 3% GA solution in pure water which was pipetted on top of the peptide hydrogel. The samples were placed in the fridge for 24 h. The GA solution was then removed and the hydrogel was rinsed twice with water. Gelatin and agar hydrogels were prepared by heating the solutions to 85 °C for 10 min and then cooling to room temperature. CTAC hydrogels were prepared by mixing 0.25 ml of a 25% CTAC solution in water and 0.25 ml of a sodium salicylate (0.1 M)–sodium chloride (0.1 M) solution in water.

Freeze-drying

Freezing the hydrogels was achieved by quickly immersing the samples in liquid nitrogen for 2 min. Once the samples were frozen they were then lyophilised in a freeze-drier (Heto, dry-winner) overnight.

Transmission electron microscopy (TEM)

Peptide hydrogels. Copper EM grids (Agar scientific) of mesh size 300 were coated with a carbon film by cleaving a piece of mica and then depositing a layer of carbon onto the surface of the mica sheet using a vacuum coating unit. The carbon-coated mica was left overnight to dry. The grids were immersed in deionised water and the carbon-coated mica was slowly immersed into the water (45° angle) allowing the mica to sink to the bottom of the container and leaving the carbon film floating on the surface of the water. The water was slowly drained and the carbon coating was deposited onto the surface of the EM grids. The grids were left overnight to dry and then glow-discharged. A droplet of 150 times diluted hydrogel was deposited onto a clean surface and a grid was placed on top of the sample droplet for 1 min. The grid was blotted dry and then negatively stained by placing the grid on top of a droplet of uranyl acetate (UA, 4% in water) for 20 s. The specimens were allowed to air-dry and the images were obtained using a Philips CM10 electron microscope at an accelerating voltage of 80 kV.

Fixed stained peptide aerogels. The peptide aerogels were each placed in a sample tube and initially fixed with 2.5% glutaraldehyde in 0.1 M phosphate buffer, for 2.5 h at room temperature. The samples were then spun down and the supernatant was removed. 0.1 M phosphate buffer was then added to the pellets, the samples were vortexed and left for 30 min; this process was repeated twice. The samples were then post fixed with 1% osmium tetroxide, vortexed and left overnight. Next day the samples were spun down and the osmium tetroxide was removed. The samples were washed by addition of 0.1 M phosphate buffer; then they were vortexed and left for 30 min; this procedure was repeated twice. Dehydration of the samples was carried out by dispersing the aerogels in an ascending alcohol series (20%, 40%, 60%, 80%, 2 × 100%), 20 min for each change. For every change the aerogels were centrifuged down so that the alcohol could be removed without losing the sample. In order to routine-embed the aerogels, the alcohol was replaced with two changes of propylene oxide (20 min each change), then replaced with a 50–50% mixture of propylene oxide–araldite overnight (using a rotator to aid infiltration), then replaced by a 75–25% mixture of araldite–propylene oxide over several hours and finally replaced with a neat fresh araldite for 3 h. New fresh araldite was added after 3 h and aerogels were polymerised overnight at 60 °C. 80–90 nm thin sections were cut using a Reichert-Jung ultracut OMU4 ultra microtome. The sections were stained with uranyl acetate (2.5 h) and lead citrate before being viewed on a Philips CM10 electron microscope at an accelerating voltage of 80 kV.

Unfixed rotary shadowed peptide aerogels. The P_{11}-2 aerogel was initially suspended in ethanol and then transferred onto a carbon film grid. The sample was then air dried and sputtered with chromium using a Cressington 208HR high-resolution sputter-coater. The thickness of the coating was set at 2.0 nm at a current of 80 mA. The samples were analysed using a CM12 transmission electron microscope operating at 120 kV.

Scanning electron microscopy (SEM)

Field emission SEM was carried out on a LEO 1530 Gemini column FEGSEM. Each aerogel sample was placed on an SEM aluminium stub and the samples were then splutter coated with

a 10 nm thick platinium/palladium coating. Imaging was carried out at an accelerating voltage of 1–3 kV.

Optical microscopy

Optical microscopy was carried out using an Olympus BH2 light microscope fitted with an Olympus SC35 camera. The samples were placed between a glass slide and cover slip and viewed through crossed-polarisers.

Fourier transform infra red (FTIR) spectroscopy

KBr pellets were prepared by mixing the aerogels with potassium bromide and pressing into disc-shaped specimens. FTIR spectra were recorded using a Thermo Scientific Nicolet 6700 FT-IR spectrometer, as averages of 64 scans at room temperature. Blank spectra were subtracted from the sample traces, the baseline corrected and the spectra smoothed. Analysis of the amide I band was carried out by band fitting using the OMNIC 7.3 software.

X-Ray diffraction

X-Ray diffraction was carried out on a PANalytical X'pert MPD diffractometer, using an angle range of 3–35° and a step size of 0.1.

X-Ray tomography

Small pieces of aerogels were placed in 2 mm diameter glass capillaries. Data were obtained at station C of the 5-BM X-ray line at Sector 5 (DND-Cat) of the Advanced Photon Source at Argonne National Laboratory, Argonne, Illinois. Each capillary was mounted and aligned vertically on a Huber goniometer mount affixed to a precision rotational stage. Samples were exposed to a parallel X-ray beam having an energy of 15.0 KeV (selected *via* a Si 111 monochromator crystal). The transmitted X-rays were imaged on a 5 μm YAG:Ce phosphor on a 500 μm undoped-YAG support. The images were captured using a Roper Scientific Cryo-Tiger-cooled VersArray CCD camera with a back-illuminated EEF36-40 1340 × 1300 CCD chip (24 μm pixel size). An optical magnification lens was used between the phosphor and the CCD camera. This configuration yielded a pixel size of roughly 2.4 × 2.4 μm^2 in the resulting images. Exposures were 8 s in duration and samples were rotated 0.15° between exposures over a 180° angular range for a total of 1200 captured images. A dark frame (no beam) was collected to correct images for camera "dark current" and a blank frame (beam on, no sample) was collected every 5 sample image frames to correct for beam non-uniformities. Reconstruction of 3D density maps was accomplished using a filtered back projection algorithm on a Beowulf cluster of 16 Pentium processors. The resulting density maps consisted of 1299 × 1299 × 1000 2-byte values, each corresponding to the X-ray density of a 2.4 × 2.4 × 2.4 μm^3 volume of space in the sample.

Compression testing

The aerogels were analysed using a floor standing, screw driven, Instron tension/compression testing machine. The compression machine was run at a rate of 5 mm/min for all samples and the appropriate load scale was chosen depending on the maximum stress of the material. The approximate aspect ratio for each sample was 1.33:1 (length/width) and the samples were compressed from approximately 12 mm to 5 mm.

Results

Hydrogels of all peptides were prepared at a concentration of 40 mg/ml (ca. 2.6% v/v), which is more than two orders of magnitude higher than the critical concentration c* for self-assembly of these peptides in water. Upon addition of water, peptide P_{11}-1 produced a clear isotropic fluid, which, over a period of four days, converted to a birefringent fluid and after approximately one week, it transformed to a clear self-supporting birefringent hydrogel (Fig. 2e). TEM established that the aggregates inside P_{11}-1 hydrogels had widths of 1–10 nm, persistence lengths of 0.2–0.3 μm and lengths of up to 100s of nm (Fig. 2a), consistent with the presence of mainly tapes and ribbons.[12] Upon addition of water to P_{11}-7, a gel was instantaneously obtained. In order to fully dissolve the peptide and produce a clear homogenous self-supporting hydrogel, heating of the peptide hydrogel was needed (80 °C for 1 min 30 s). This allowed the inhomogeneous hydrogel to return to the monomeric fluid state and, upon cooling, clear self-supporting birefringent hydrogels were obtained. TEM of P_{11}-7 hydrogel showed aggregates with widths of 5–10 nm, persistence lengths of 0.1–0.2 μm and total lengths of >0.4 μm, in agreement with the expected presence of thin fibrils (Fig. 2b). Addition of water to P_{11}-2 produced strong hydrogels within minutes. These hydrogels were slightly cloudy and strongly birefringent (Fig. 2e). The gel consisted of aggregates with wide widths (w/w) of 12–15 nm, narrow widths (n/w) of 4–6 nm, twist pitch (one full length) of 130–180 nm, persistence lengths of 20–60 μm and total lengths of >1.9 μm (Fig. 2c), in accordance with the presence of well-defined fibrils.[12] PolyT was also studied to compare its behaviour with the short self-assembling peptides. PolyT addition in water produced semi transparent, non-birefringent, yellow self-supporting hydrogels in aqueous solutions over a time period of approximately two weeks. The yellow colour is possibly due to the presence of traces of impurities in the peptide. TEM of polyT hydrogel revealed ribbons with diameters of 2–4 nm, persistence lengths of ca. 20–60 nm and total lengths of >1.5 μm (Fig. 2d). Fibrils occasionally entwined around each other to produce fibres, as can be seen in several peptide samples (Fig. 2b and c).

Following lyophilisation, all hydrogels converted to white, light materials *i.e.* aerogels, retaining the integrity, shape and most of the volume of the starting hydrogels (Fig. 3a, inset). When cut open, they revealed an inner radial pattern (Fig. 7). SEM examination of P_{11}-1 exposed an anisotropic, flat, lamellar-like structure with thickness of 1.5–2.5 μm and width of 30–100 μm; lamella stacked on top of each other with gaps of 5–15 μm between them (Fig. 3a and b). Similar SEM data were obtained for all peptide aerogels (ESI, Fig. S1‡); the lamella had widths in the range 20–200 μm and the gaps between them were 5–40 μm in length. In some cases the lamella were seen to form honeycomb-like or leaf-like structures (ESI, Fig. S1‡). Freeze-drying of self-assembling hydrogels based on polysaccharide agar and CTAC surfactant rod-like micelles[34] was also carried out for

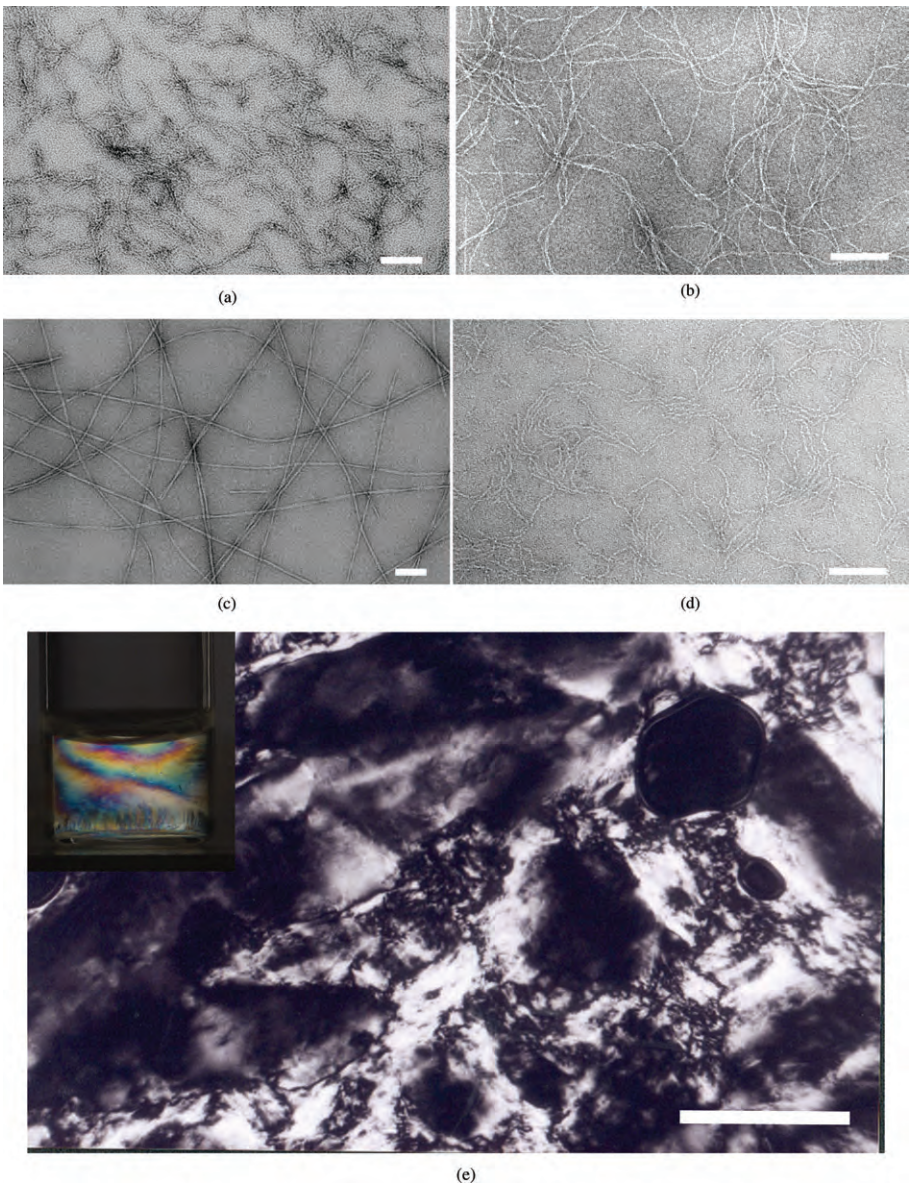

Fig. 2 TEM micrographs of peptide hydrogels (a) P_{11}-1, (b) P_{11}-7, (c) P_{11}-2, (d) poly-L-threonine at a concentration of 40 mg/ml in water; scale bars represent 100 nm. (e) Polarised optical micrograph of a P_{11}-1 hydrogel at a concentration of 40 mg/ml in water taken with an aliquot of gel between a microscope slid and a coverslip; scale bar = 400 μm. Inset: Strongly birefringent, nematic liquid crystal P_{11}-2 hydrogel at a concentration of 5 mg/ml.

comparison. Agar aerogel produced an open isotropic 3 dimensional network of suprafibres with widths of 0.2–1.5 μm and average pore sizes of 5–15 μm (Fig. 3c), whilst the CTAC network collapsed after lyophilisation and produced compact aggregates (Fig. 3d). X-Ray tomography is a lower resolution technique compared to SEM, but it allows examination of both the interior and the exterior morphology of a sample, thus it was employed in a complementary manner to SEM. A typical X-ray tomography image of a single fragment of P_{11}-2 aerogel (Fig. 4a) at a concentration of 80 mg/ml showed a highly anisotropic structure of thin linear structures most likely corresponding to the edge-on views of individual lamella with a gap between each sheet of ca. 24 μm. Similar X-ray tomography images were collected for P_{11}-1, P_{11}-7 and polyT (ESI, Fig. S2‡), although these samples were more fragmented compared to P_{11}-2 (Fig. 4a). All the frames were combined to produce movies of the internal architectures of the aerogels. A movie of P_{11}-2 comprising two main aerogel fragments can be found in the ESI (Movie 1‡) and a snapshot of the movie can be seen in Fig. 4b. The stacks of flat lamellar structures are clearly seen, in full agreement with the SEM data. A movie comprising several pieces of polyT aerogel can also be seen in the ESI (Movie 2‡) and a snapshot of the movie in Fig. 4d. At closer inspection, the lamellar structures appear to consist of long thin aggregates packed together. In contrast to the highly anisotropic structure of the peptide X-ray tomography image (Fig. 4a), the X-ray tomography of agar aerogel revealed an isotropic porous structure throughout (Fig. 4c), consistent with its SEM image (Fig. 3c).

TEM of unfixed P_{11}-2 aerogel revealed the presence of well-defined, semi-rigid aggregates with widths of approximately 10

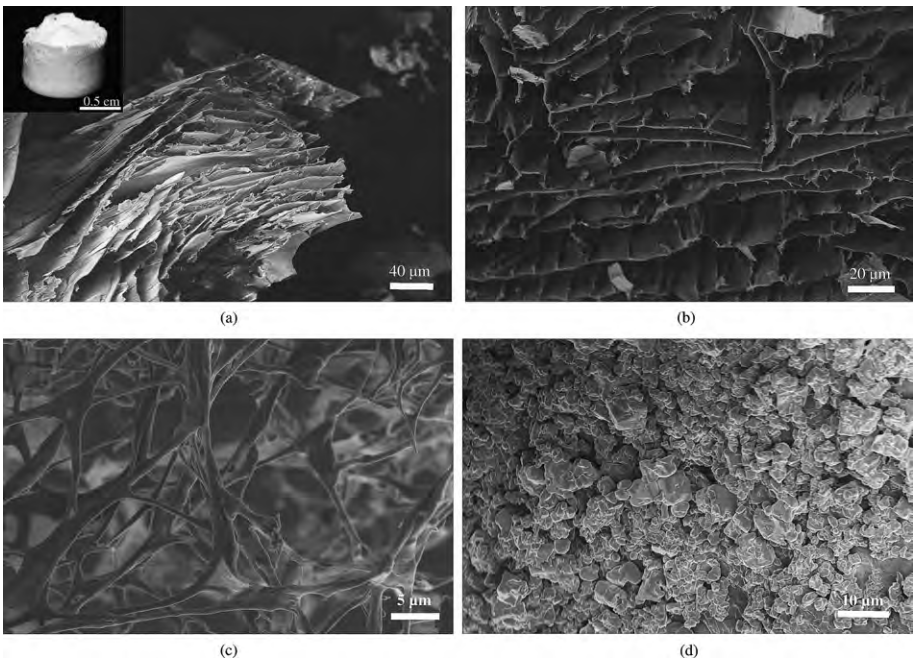

Fig. 3 Scanning electron micrographs of freeze-dried samples: (a and b) P_{11}-1 aerogel at a concentration of 2.6% (40 mg/ml); inset: photograph of a P_{11}-1 aerogel (2.6%) after freeze-drying; (c) agar aerogel at a concentration of 2.6% (40 mg/ml); (d) CTAC surfactant rod-like micelles at a concentration of 12.5%.

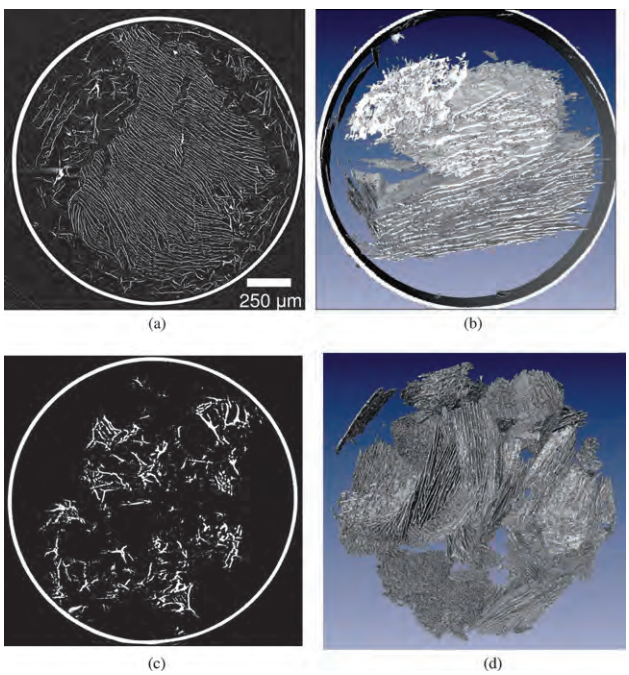

Fig. 4 X-Ray tomography snapshots of the internal structure of freeze-dried aerogels: (a) a fragment of P_{11}-2 aerogel at 80 mg/ml; (b) snapshot of a 3D movie representation of the internal structure of two main pieces of P_{11}-2 aerogel; (c) agar aerogel at 80 mg/ml; (d) snapshot of a 3D movie representation of the internal structure of several pieces of poly-L-threonine aerogel at 75 mg/ml; outer diameter of circles = 2 mm.

nm and lengths of μm (Fig. 5a), reminiscent of the morphology of P_{11}-2 fibrils in the starting hydrogel. In order to establish the arrangement of the fibrils within the lamellar structure of the aerogel, the aerogel was fixed and examined by TEM. The fibrils appeared like thin, rigid needle-like black lines, each several hundred nm in length (Fig. 5b). Several dozen to hundreds of fibrils aligned next to each other to form mesoscopic nematic-like domains with widths of 100–200 nm and lengths of μm (Fig. 5b). The orientation of the fibrils was similar within each domain, but different from domain to domain. TEM of unfixed P_{11}-1 aerogel showed that it was made of short, thin aggregates with widths of 3–5 nm (data not shown), indicative of the morphology of the P_{11}-1 ribbons in the starting hydrogel. TEM of fixed P_{11}-1 aerogels again established the presence of local nematic-like ordering of the ribbons into domains with widths of 150–400 μm and lengths of the order of microns (data not shown). Powder X-ray diffraction revealed sharp peaks corresponding to a periodicity of 0.45–0.48 nm, diagnostic of the peptide-peptide separation in a β-sheet tape for all three peptide aerogels (ESI, Fig. S3‡). Another broader peak corresponding to a periodicity of 0.83–1.02 nm may be attributed to tape thickness in stacks of tapes, whilst an even broader peak corresponding to a repeat of 1.97 nm could be due to the ribbon thickness in stacks of ribbons.[35] FTIR spectra of all peptide aerogels revealed the predominant presence of β-sheet structure[52] (ESI, Fig. S4‡).

Compression testing was carried out on the peptide aerogels and the results were compared with similar aerogels made of gelatine or agar (Fig. 6a). Gelatine and agar aerogels produced curves which are reminiscent of porous materials in compression.[36] They have an initial linear-elastic region followed by the compression zone and then onto the densification region. The modulus of each aerogel was measured in the linear-elastic region. P_{11}-7 aerogel had an average compression modulus of 0.05 MPa, which was 11 times lower, compared to that of agar aerogel and 15 times lower compared to gelatine aerogel (Fig. 6b). Preliminary measurements of P_{11}-2, P_{11}-1 and polyT

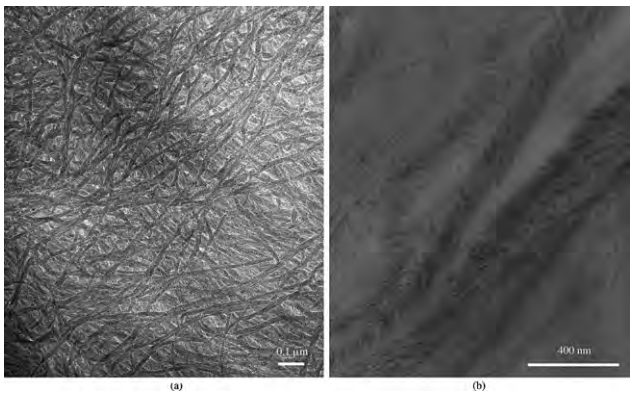

Fig. 5 TEM micrographs of (a) rotary shadowed unfixed P_{11}-2 aerogel and (b) UA stained fixed P_{11}-2 aerogel at 40 mg/ml.

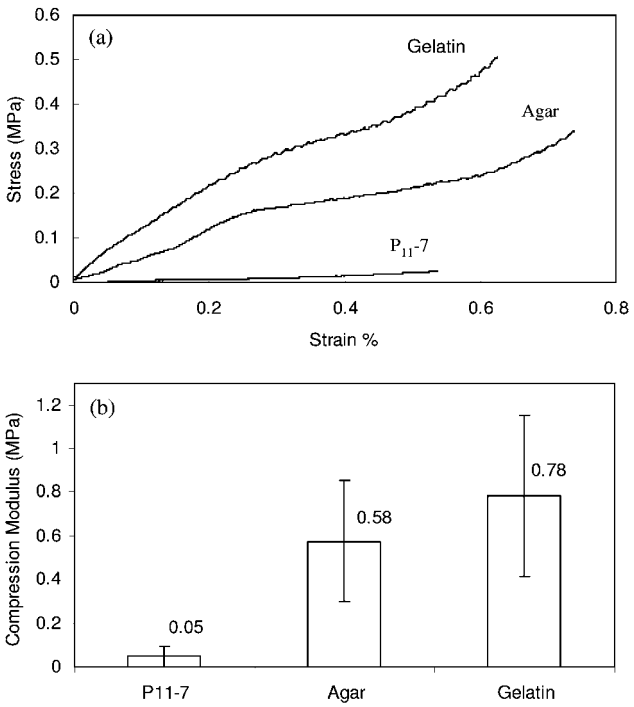

Fig. 6 (a) Typical compression curves of gelatin, agar and P_{11}-7 aerogels and (b) bar chart illustrating the average compression modulus and standard deviation of P_{11}-7, agar and gelatin at 40 mg/ml.

aerogels suggested that they had similar mechanical properties to P_{11}-7. In a first attempt to improve the mechanical strength of the peptide aerogels, pilot studies were carried out with glutaraldehyde (GA), known to cross-link materials with amine groups.[37] For these experiments, aerogels were prepared using variants of P_{11}-2 bearing ornithine side chains which contain free amines, such as P_{11}-8 (Table 1). However no improvement in mechanical strength was observed by compression testing of these peptide aerogels compared to the non GA-treated ones. This may be due to the close packing of the peptide side chains inside the β-sheet tapes and fibrils, rendering them largely inaccessible to water-soluble cross-linking compounds such as GA. Alternatively the modulus may not be governed by the integrity of the β-sheets at all but rather by their bending modulus or the torsional modulus of the junctions. The solubility of the peptide aerogels P_{11}-7 and P_{11}-2 at a conc. of 80 mg/ml was also tested at room temperature by placing them in a large volume of water or methanol. Both aerogels dissolved fully within a matter of 2 h. Aggregates made of complementary peptides are considered to be more stable in general. Aerogels were made of complementary peptides P_{11}-4/P_{11}-5[14,15] which are variants of P_{11}-2 (Table 1). The aerogels sank to the bottom of the vials by taking in the solvent, but remained largely intact in contact with bulk solvent for at least 5 d in both water and methanol at room temperature. Aerogels of P_{11}-4, P_{11}-8 or complementary peptides were also placed in DMEM aq. solution which is the basis of cell culture media at room temperature. They took in solvent but remained intact for 18 months. An aerogel of P_{11}-4 was further placed in DMEM at 37 °C and remained intact for at least 10 d.

Discussion

We have studied the behaviour of three short *de novo* designed self-assembling peptides P_{11}-1, P_{11}-2 and P_{11}-7 and their variants. P_{11}-1 formed ribbons at high concentrations in water, whilst P_{11}-7 and P_{11}-2 gave rise to thin and thicker fibrils respectively. All three peptides produced birefringent gels at 40 mg/ml, due to the alignment of their aggregates into ordered micro-domains. The homopolypeptide polyT also self-assembled into ribbon-like structures in water giving rise to non-birefringent hydrogels. Freeze-drying of the peptide hydrogels using liquid N_2, produced light white porous materials (aerogels) with an inner radial pattern (Fig. 7). SEM and X-ray tomography revealed that in all cases the aerogels consisted of extensive aligned flat lamellar structures that formed macroscopically oriented domains of mm dimensions (Fig. 4a), sometimes also seen to arrange into honeycomb or leaf-like patterns. The lamellar porous materials are templated between growing ice crystals with a columnar or lamellar morphology.[22] Columnar ice forms at the sample that is nearer the cooling interface; this may give rise to lamellae of materials which are not parallel to each other, possibly giving rise to micro-honeycomb and other architectures. Lamellar ice forms further inside the sample; this may further order the peptide lamellae parallel to each other.[38] It is not surprising that different peptide nanostructures may give rise to similar lamellar architectures following freeze-drying, since the process depends largely on physical rather than chemical principles.[22] On the basis

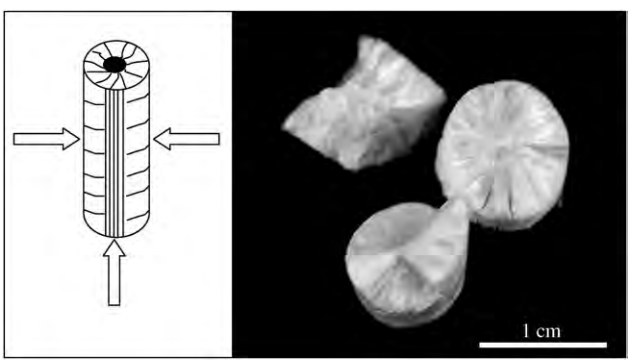

Fig. 7 Illustration of the effect of ice crystallisation on hydrogel structure and a photograph of a P_{11}-2 aerogel at 40 mg/ml after lyophilisation, demonstrating the resulting inner radial pattern.

of previous TEM of slices of cross-linked hydrogels[13] and optical microscopy of stained hydrogel networks,[39] it would appear that the lamellar architecture is not present in the starting hydrogel state, but it is rather the result of the freezing process.

Mechanical testing revealed low compression modulus *i.e.* the peptide aerogels are brittle compared to the well-known agar and gelatine aerogels. The poor mechanical performance may be due to the underlying lamella structure; rigid flat structures may not be the ideal components for the formation of strong networks since they are susceptible to bending/buckling-mode deformations resisted in networks by other rigid components such as walls.[40] Another possible reason for the poor mechanical properties of the peptide aerogels is the brittleness of the peptide fibrils. Furthermore the peptide chains are very short compared to agar and gelatine chains, and are held together by non-covalent interactions, which may make their lamella easy to break under pressure. Despite this, solubility tests revealed that the peptide aerogels absorbed solvent but remained intact for a considerable amount of time, depending on the peptide chemical structure and the solvent, e.g. in the presence of a large volume of aq. biological solutions.

During freezing, hexagonal ice crystallisation in the form of platelets takes place rejecting the peptide nanostructures at the spaces between crystals, due to the very low solubility limit of ice to impurities.[22] Formation of dendrites on the ice crystals gives rise to roughness on the surface of the peptide lamellae. The ice platelets form simultaneously everywhere on the inner cold surfaces of the side walls and bottom of the tube and proceed inwards meeting at the centre of the material, thus giving rise to the observed radial pattern (Fig. 7). The resulting peptide lamellar architecture is a replica of the ice platelets during freezing, and thus should be present in the frozen hydrogel, with little influence of the subsequent sublimation process.[22] The radial pattern was not observed in the peptide aerogels when controlled freezing[24] and directional ice crystallisation took place only from the bottom of the tube upwards and not from its sides (data not shown). Similar radial supramolecular structures have also been observed by others upon the crystallisation of the solvent.[41] The growth of ice platelets seems to partly break the peptide network and push the nematic micro-domains of aligned peptide aggregates present in the hydrogel out of the ice phase, partially align them with each other and compress them in very high concentrations at the peripheries of the ice crystals; thus the ice crystals template the observed lamellar structures and the pores of the aerogel (Fig. 1). Flat, leaf-like structures were observed before in polymer and biopolymer aerogels as well as in inorganic materials after freeze-drying and were also attributed to solvent crystallisation.[23,42–50]

We might expect that the massive increase of peptide concentration during ice crystallisation would cause a transition of the peptide nanostructures into higher order aggregates, thus the ribbons might convert into fibrils and the fibrils into fibres. This is not observed though, instead the peptide nanostructures present in water appeared to be unaltered by freeze-drying. Peptide aerogels consisted predominantly of β-sheet structure as established by FTIR and X-ray diffraction, behaviour consistent with their starting hydrogel states. In addition P_{11}-2 aerogel comprised typical P_{11}-2 fibrils, whilst P_{11}-1 aerogel contained thinner aggregates consistent with the presence of ribbons as in the case of P_{11}-1 hydrogel. Furthermore TEM of fixed peptide aerogels implied the ribbons and fibrils were ordered into extensive mesoscopic nematic-like domains, again as in the case of the starting hydrogels. It is possible that the intrinsic twist of the peptide aggregates prevents their conversion into higher order structures during ice growth. Another possibility is that the high scission energy of the peptide aggregates[12] may kinetically stabilise them, i.e. there may not be enough time for the peptide aggregates to convert to higher order structures during the rapid ice growth, thus they are locked in their original state.

However not all self-assembling networks behave in the same manner. It was observed for example in the present study that unlike the behaviour of the peptides, freeze-drying of a hydrogel of self-assembling CTAC surfactant rod-like micelles caused collapse of its 3D structure, coagulation of the surfactant into solid particles and the absence of any lamella (Fig. 3d). This may be ascribed to the particularly weak nature of the network of the rod-like micelles that may be completely smashed by ice growth; another possible explanation is that during water freezing the concentration of CTAC increases massively, which may drive the transition of the rod-like micelles into a different self-assembling state e.g. crystal structure; this is unlike the more robust peptide aggregates that appear unaffected by freeze-drying. In contrast to CTAC, strong hydrogel networks, such as agar, seem to be able to resist the reorganisation brought about by ice crystallisation, and possibly even inhibit the growth of ice crystals; this results in the preservation of the isotropic, fibrous architecture of the hydrogel network even after freeze-drying (Fig. 3c), with little inner radial pattern present, and again absence of lamellar arcitecture. Thus the differences in the physical and chemical properties of the self-assembling network seem to prescribe the way it will behave during ice crystallisation, and whether or not it will form lamellar structures.

A fundamental question concerns the emergence of the lamellar structures, rather than any other morphology in which the peptide material is excluded from the regions occupied by the crystallised solute. We believe that there are rather close similarities between this system and that of other polymeric lamella-forming structures such as block-co-polymer mesophases (BCPs).[51] When BCPs form lamella, they do so because curvature of the interfaces between the regions dominated by either component carries a strong free energy penalty. Once strongly phase-separated, the same will be true of domains formed by aggregated peptide ribbons or fibrils, such as our observations show. Since the fibrillar structure is retained in the lamella, they inherit the strong persistence (resistance to bending) of the linear assemblies themselves. But if we understand how "late-stage" phase separation may arrive at lamella, we still need to explain their regular spacing. This is likely to be templated at an early-stage of separation during the crystallisation process, setting a characteristic length scale of composition fluctuations before non-linear effects such as curvature-suppression mould these into lamella. A well-known example of this phenomenon is the "spinodal decomposition" of polymer blends, by which a dominant length scale arises at a fastest-growing wavelength of spatially-periodic fluctuation in composition. In the Appendix, we show that the system of peptide, solute and crystal may actually give rise to a dynamic composition instability formally identical to spinodal decomposition at the mean-field level. Two couplings are required: (1) a dependence of solute crystal growth

rate on local peptide concentration; (2) a flux of peptide driven out of regions in which the crystals are growing fastest. Both of these are generically present. One attractive feature of this scenario is that it suggests control routes for the lamellar spacing, since the dominant wavelength is dependent on the product of the two coupling strengths. Verifying this prediction is an attractive task for future work. We may also speculate that other consequences of an early-stage spinodal-like growth are represented by the "leaf-like" and other structures perpendicular to the dominant lamella, as seen in Fig. 3 and Fig. S1 (ESI‡).

The present study demonstrates that ice formation during lyophilisation does not appear to affect the self-assembling peptide nanostructures, but it can effectively order them into stacked lamella over the mm lengthscale. Further optimisation of macroscopic alignment may be achieved by influencing the direction of ice crystallisation. Optimisation of morphological length scales may likewise be controlled by modifications of the interaction of the peptide nanostructures and growing ice crystals. A detailed understanding of the relationship between freezing conditions in FD and the resulting microstructure has begun, which will lead to fine tuning of the material properties,[22,23] e.g. the %porosity can be controlled by solute concentration, the pore dimensions by freezing kinetics, homogeneous freezing results in long range order of the lamellar structure, whilst other treatments produce radially oriented porosity or more complicated patterns. Both alignment and morphology are important for high-resolution structural X-ray diffraction studies that rely on well-aligned samples; anisotropic microporous materials comprising lamellar-like layers of self-assembling peptide fibrils with incorporated protein-like bioactivity may also be useful in medical applications e.g. tissue engineering and nanotechnology.

Appendix: spinodal instability and lamellar structures from the solute crystal nucleation rate

The development of morphology from solvent crystallisation in a self-assembled peptide gel, just as in other examples of driven phase-separation in polymeric fluids, is controlled by both early-stage and late-stage growth of the composition fluctuations. The self-assembled peptides act as persistent polymers, possessing the usual attributes of a correlation length ξ and compositional diffusion constant D which on their own generate dynamics for the polymer composition fluctuations $\delta\phi_p(r,t)$:

$$\delta\dot{\phi}_p = D[\nabla^2 + \xi^2\nabla^4]\delta\phi_p(r,t)$$

The RHS may be thought of as the divergence of a polymer flux with two components, a diffusive flux $j_D = -D\nabla\delta\phi_p$ driven by concentration gradients, and a conformational flux $j_c = -D\nabla\frac{\xi^2}{2}(\nabla\delta\phi_p)^2$ driven by density correlations of the polymer field. In the case where the solute is crystallising, there will be an additional component to the polymer flux generated by the exclusion of the polymer by the growing crystals. If the crystal growth rate $\dot{\rho}_x(r,t)$ is higher in one region than a neighbouring one, a current of the form $j_x = -\Gamma\nabla\dot{\rho}_x(r,t)$ will additionally contribute to the polymer flux.

The presence of polymers in solution may, in turn, strongly suppress the nucleation of crystallisation of the solute, either by direct suppression of nucleation, or by modifying the growth rate. In either case the linear-response regime of the growth rate will track that of the polymer composition fluctuations so that

$$\nabla\dot{\rho}_x(r,t) = -\eta\nabla\delta\phi_p$$

When the coupling to crystallisation is added to the composition dynamics, the resulting phenomenology,

$$\delta\dot{\phi}_p = D[(1 - \lambda\Gamma)\nabla^2 + \xi^2\nabla^4]\delta\phi_p(r,t)$$

is identical to the Cahn-Hilliard growth equation for spinodal instabilities in the phase-separating region. The consequences in the linear-response regime are well-known: in particular the early-stage morphology is dominated by a fastest-growing wavelength of fluctuations

$$\lambda_{\max} = 2\pi\sqrt{\frac{2\xi^2}{(\eta\Gamma - 1)}}$$

The condition for unstable growth of peptide concentrations is that $(\eta\Gamma - 1) > 0$, *i.e.* that the product of the couplings of crystal growth rate to excluded peptide flux, and of peptide concentration to crystallisation growth rate, is large enough.

Late stage growth to lamellar morphology is a consequence of the persistence of the fibrils and ribbons, as discussed in the text.

Acknowledgements

We gratefully acknowledge the financial contribution of Dow Benelux BV, Royal Society for the award of a University Research Fellowship to AA and the Dutch Polymer Institute. The help of Mr Martin Fuller with fixation procedures is also appreciated. X-Ray tomography was performed at the DuPont-Northwestern-Dow Collaborative Access Team (DND-CAT) Synchrotron Research Centre located at Sector 5 of the Advanced Photon Source. DND-CAT is supported by the E.I. DuPont de Nemours & Co., the Dow Chemical Company, the U.S. National Science Foundation through Grant DMR-9304725 and the State of Illinois through the Department of Commerce and the Board of Higher Education Grant IBHE HECA NWU 96. Use of the Advanced Photon Source was supported by the U. S. Department of Energy, Office of Science, Office of Basic Energy Sciences, under Contract No. W-31-109-Eng-38.

References

1 R. P. W. Davies, A. Aggeli, A. J. Beevers, N. Boden, L. M. Carrick, C. W. G. Fishwick, T. C. B. McLeish, I. Nyrkova and A. N. Semenov, *Supramol. Chem.*, 2006, **18**, 435–443.
2 S. Stupp, *MRS Bulletin*, 2005, **30**, 864–873.
3 S. Zhang, *Biotechnology Advances*, 2002, **20**, 321–339.
4 R. J. Mart, R. D. Osborne, M. M. Stevens and R. V. Ulijn, *Soft Matter*, 2006, **2**, 822–835.
5 J. P. Schneider, D. J. Pochan, B. Ozbas, K. Rajagopal, L. Pakstis and J. Kretsinger, *J. Am. Chem. Soc.*, 2002, **124**, 15030–15037.
6 S. Scanlon and A. Aggeli, *Nano Today*, 2008, **3**, 22–30.
7 H. G. Borner and H. Schlaad, *Soft Matter*, 2007, **3**, 394–408.
8 H. A. Klok, *J. Polym. Sci. Pol. Chem.*, 2005, **43**, 1–17.
9 H. A. Klok and S. Lecommandoux, in *Peptide Hybrid Polymers*, Springer-Verlag Berlin, Berlin, 2006, vol. 202, pp. 75–111.

10 J. C. M. van Hest and D. A. Tirrell, *Chem. Commun.*, 2001, 1897–1904.
11 M. Fandrich and C. Dobson, *The EMBO Journal*, 2002, **21**, 5682–5690.
12 A. Aggeli, I. A. Nyrkova, M. Bell, R. Harding, L. Carrick, T. C. B. McLeish, A. N. Semenov and N. Boden, *Proc. Natl. Acad. Sci. USA*, 2001, **98**, 11857–11862.
13 A. Firth, A. Aggeli, J. L. Burke, X. B. Yang and J. Kirkham, *Nanomedicine*, 2006, **1**, 189–199.
14 A. Aggeli, M. Bell, N. Boden, L. M. Carrick and A. E. Strong, *Angew. Chem.-Int. Edit.*, 2003, **42**, 5603–5606.
15 A. Aggeli, M. Bell, L. M. Carrick, C. W. G. Fishwick, R. Harding, P. J. Mawer, S. E. Radford, A. E. Strong and N. Boden, *J. Am. Chem. Soc.*, 2003, **125**, 9619–9628.
16 L. M. Carrick, A. Aggeli, N. Boden, J. Fisher, E. Ingham and T. A. Waigh, *Tetrahedron*, 2007, **63**, 7457–7467.
17 J. E. Meegan, A. Aggeli, N. Boden, R. Brydson, A. P. Brown, L. Carrick, A. R. Brough, A. Hussain and R. J. Ansell, *Advanced Functional Materials*, 2004, **14**, 31–37.
18 J. Kirkham, A. Firth, D. Vernals, N. Boden, C. Robinson, R. C. Shore, S. J. Brookes and A. Aggeli, *J. Dent. Res.*, 2007, **86**, 426–430.
19 C. Whitehouse, J. Y. Fang, A. Aggeli, M. Bell, R. Brydson, C. W. G. Fishwick, J. R. Henderson, C. M. Knobler, R. W. Owens, N. H. Thomson, D. A. Smith and N. Boden, *Angew. Chem.-Int. Edit.*, 2005, **44**, 1965–1968.
20 C. J. Bell, L. M. Carrick, J. Katta, Z. M. Jin, E. Ingham, A. Aggeli, N. Boden, T. A. Waigh and J. Fisher, *J. Biomed. Mater. Res. Part A*, 2006, **78A**, 236–246.
21 S. Scanlon, A. Aggeli, N. Boden, R. J. Koopmans, R. Brydson and C. M. Rayner, *Micro & Nano Letters*, 2007, **2**, 24–29.
22 S. Deville, E. Saiz and A. P. Tomsia, *Acta Materialia*, 2007, **55**, 1965–1974.
23 S. Deville, E. Saiz, R. K. Nalla and A. P. Tomsia, *Science*, 2006, **311**, 515–518.
24 P. X. Ma and R. Zhang, *J. Biomed. Mater. Res.*, 2001, **56**, 469–477.
25 F. M. Plieva, M. Karlsson, M. R. Aguilar, D. Gomez, S. Mikhalovsky and I. Y. Galaev, *Soft Matter*, 2005, **1**, 303–309.
26 V. P. Shastri, I. Martin and R. Langer, *Proceedings of the National Academy of Sciences*, 2000, **97**, 1970–1975.
27 H. F. Zhang and A. I. Cooper, *Soft Matter*, 2005, **1**, 107–113.
28 M. Power, B. Hosticka, E. Black, C. Daitch and P. Norris, *Journal of non crystalline solids*, 2001, **285**, 303–308.
29 J. Lee, *J. Mater. Sci.*, 1997, **32**, 5825–5832.
30 Z. Zhao and H. Matsui, *Small*, 2007, **3**, 1390–1393.
31 X. M. H. Huang, R. Caldwell, L. M. Huang, S. C. Jun, M. Y. Huang, M. Y. Sfeir, S. P. O'Brien and J. Hone, *Nano Lett.*, 2005, **5**, 1515–1518.
32 S. O. Lumsdon, E. W. Kaler and O. D. Velev, *Langmuir*, 2004, **20**, 2108–2116.
33 S. G. Rao, L. Huang, W. Setyawan and S. H. Hong, *Nature*, 2003, **425**, 36–37.
34 A. T. Hubbard, *Encyclopedia of Surface and Colloid Science*, CRC Press, 2002.
35 B. W. Matthews, *X-ray Structure of Proteins*, vol. 3, Academic Press, New York, 1977.
36 L. J. Gibson and M. F. Ashby, *Cellular Solids*, Pergamon Press, Oxford, 1988.
37 I. Rault, V. Frei, D. Herbage, N. AbdulMalak and A. Huc, *J. Mater. Sci.-Mater. Med.*, 1996, **7**, 215–221.
38 M. C. Gutiérrez, M. L. Ferrer and F. del Monte, *Chem. Mater.*, 2008, **20**, 634–648.
39 S. Felton, PhD thesis, University of Leeds, Leeds, UK, 2006.
40 D. J. Read, R. A. Duckett, J. Sweeney and T. C. B. McLeish, *J. Phys. D-Appl. Phys.*, 1999, **32**, 2087–2099.
41 J. Zhang, B. Berge, F. Meeussen, E. Nies, H. Berghmans and D. Shen, *Macromolecules*, 2003, **36**, 9145–9153.
42 S. Blacher, V. Maquet, R. Jerome and J. P. Pirard, *Image Anal Stereol*, 2002, **21**, 43–48.
43 S. Blacher, V. Maquet, R. Pirard, J. P. Pirard and R. Jerome, *Colloids and Surfaces A: Physicochemical and Engineering Aspects*, 2001, **187–188**, 375–383.
44 S. Deville, E. Saiz and A. P. Tomsia, *Biomaterials*, 2006, **27**, 5480–5489.
45 H. W. Kang, *Biomaterials*, 1999, **20**, 1339–1344.
46 M. Li, Z. Wu, C. Zhang, S. Lu, S. Yan, D. Huang and H. Ye, *J. Appl. Polym. Sci.*, 2001, **79**, 2192–2199.
47 S. V. Madihally and H. W. T. Matthew, *Biomaterials*, 1999, **20**, 1133–1142.
48 R. Nazarov, H.-J. Jin and D. Kaplan, *Biomacromolecules*, 2004, **5**, 718–726.
49 S. N. Park, J. C. Park, H. O. Kim, M. J. Song and H. Suh, *Biomaterials*, 2002, **23**, 1205–1212.
50 G. W. Scherer, *Journal of non crystalline solids*, 1993, **155**, 1–25.
51 M. W. Matsen, *J. Phys.-Condes. Matter*, 2002, **14**, R21–R47.
52 H. Susi, in *Methods in Enzymology*, Academic Press, 1972, vol. 26, pp. 455–472.

